

1 **3-D Crustal Shear Wave Velocity Model Derived from**
2 **the Adjoint Waveform Tomography in the Central**
3 **Japan Island**

4 **Kota Mukumoto¹, Takeshi Tsuji^{1,2}**

5 ¹Department of Earth Resources Engineering, Kyushu University, Fukuoka, Japan

6 ²International Institute for Carbon-Neutral Energy Research (I2CNER), Kyushu University, Fukuoka,
7 Japan

8 **Key Points:**

- 9 • Full waveform tomography based on the adjoint method is used to resolve the shear-
10 wave velocity structures of crust in central Japan.
11 • One of the most densely spaced seismic monitoring network of Japan, for first time,
12 is used for adjoint waveform tomography.
13 • Prominent anomalies of shear-wave velocity resolved by adjoint waveform tomog-
14 raphy reflect geological blocks of Japan and volcanic fluids.

Corresponding author: Kota Mukumoto, k.Mukumoto@mine.kyushu-u.ac.jp

Abstract

Adjoint waveform tomography, which is an emerging seismic imaging method for the crust- and global-scale problems, has gained popularity in the past and present decade. This study, for first time, applies adjoint waveform tomography to the large volume of seismic data recorded by the densely spaced, permanent monitoring network that covers the entirety of Japan. We develop a heterogeneous shear-wave velocity model of central Japan that agrees with the geology and lithology. The results reduce the time-frequency phase misfit by 16.2% in the 0.033–0.1 Hz frequency band and 3.6% in the 0.033–0.125 Hz band, respectively. We infer that some velocity anomalies resolved in this work reflect the volcanic fluids, thick sedimentary basins, and granitic rocks. The results of this study suggest the possibility of imaging heterogeneous subsurface structures around Japan island using waveform tomography with a densely distributed network of permanent seismometers.

Plain Language Summary

The complex geological structures of central Japan due to the plate interactions have gained many attentions and been subject of many previous geophysical studies. Studies of seismic structures have been mainly investigated using first-arrivals of earthquake waveforms or ambient noise wavefield. However, different methods could yield different seismic tomographic images. This is due to the differences of the limitations of methods and the data set. Therefore, estimating subsurface structures using different methods is important for better understanding of the earth's structures. Here we build shear-wave velocity model of central Japan by applying adjoint waveform tomography to the large volume of seismic data recorded by the densely spaced, permanent seismic monitoring network. The shear wave velocity model estimated by this study can yield the similar simulated waveforms of earthquakes to observed waveforms and this means that our velocity model has high accuracy. Some velocity anomalies resolved in this study are different features from previous studies. The results of this study suggest the possibility of imaging heterogeneous subsurface structures around Japan island using waveform tomography with a densely distributed network of permanent seismometers.

1 Introduction

The island nation of Japan is located on the convergent boundary where the Philippine Sea plate and the Pacific plate are subducting beneath the Eurasian and the Okhotsk plates. The interactions of these four plates are responsible for many of Japan's unique tectonic features. The boundary between the Pacific and Eurasian plates on land is the Itoigawa–Shizuoka tectonic line (ISTL), which extends from Itoigawa city in Niigata prefecture to Shizuoka city in Shizuoka prefecture. The subduction of the Philippine Sea Plate created the Izu–Bonin (arc–arc) collision zone (IBCZ), where the Izu–Bonin arc has collided with the Honshu arc. The area also includes two prominent structural features: the Median tectonic line (MTL) and the Niigata–Kobe tectonic line (NKTL).

Central Japan contains many active volcanoes, sedimentary basins, the IBCZ, and several major tectonic lines (ISTL, MTL, and NKTL). Therefore, the seismic structure of the region is expected to contain substantial lateral heterogeneities. The complex geological structures of central Japan have been the subject of many previous geophysical studies, which have relied mainly on regional- and exploration-scale seismic tomography (Arai et al., 2013; Arai & Iwasaki, 2014; J. Nakajima & Hasegawa, 2007a, 2007b; Nishida et al., 2008; Nimiya et al., 2020). For example, a series of studies using first-arrival tomography (J. Nakajima & Hasegawa, 2007a, 2007b; J. Nakajima et al., 2009) revealed the slab geometry of the Philippine Sea Plate and investigated plausible relationships between the arc magmatism and the subducting oceanic plates. Nishida et al. (2008) and Nimiya et al. (2020) leveraged the ambient noise wavefield using seismic interference and

65 clearly imaged underground structures including magmatic fluids and thick sedimentary
66 successions.

67 Recently, the development of adjoint waveform tomography techniques has improved
68 our ability to resolve subsurface structures (Fichtner et al., 2010; Tape et al., 2010; Simuté
69 et al., 2016; Lei et al., 2020). In this method, three-dimensional (3D) sensitivity distri-
70 butions of seismic waves can be computed by full numerical seismic wave simulation in
71 heterogeneous media using the adjoint method (Fichtner, 2010; Peter et al., 2011). Fur-
72 thermore, first-arrival tomography and ambient noise tomography use specific seismic
73 phases, whereas adjoint waveform tomography can use as much waveform information
74 as possible without requiring selections of seismic phases. Therefore, the application of
75 adjoint waveform tomography might improve tomographic imaging of heterogeneous seis-
76 mic velocity structures beneath central Japan.

77 The goals of the present work are to resolve crustal S-wave velocity structures in
78 central Japan based on adjoint waveform tomography, and to investigate whether it is
79 possible to obtain detailed tomographic images comparable to those resolved by other
80 popular methods (e.g., first-arrival or ambient noise tomography). Our study differs from
81 previous applications of adjoint waveform tomography in Japan (Miyoshi et al., 2017),
82 in that our target is a larger area and we use many more seismic stations. Here, we ap-
83 ply adjoint waveform tomography to the large volume of seismic data collected by Hi-
84 net (Okada et al., 2004). The estimated crustal S-wave velocity model reaches a min-
85 imum misfit after 12 iterations and shows strong lateral velocity variations. The veloc-
86 ity anomalies in the estimated model are in good agreement with the geology.

87 2 Data

88 Earthquake waveform data were collected from the Hi-net high-sensitivity seismo-
89 graph network, operated across Japan by the National Research Institute for Earth Sci-
90 ence and Disaster Prevention (NIED) (Okada et al., 2004). There are 358 Hi-net per-
91 manent stations in our study area (Figure1(a)), all have three-component velocity seis-
92 mometers and are deployed in boreholes. The seismometers are designed to have sen-
93 sitivities >1.0 Hz; however, our target frequency range is 0.033–0.125 Hz. Therefore, we
94 applied the sensitivity corrections proposed by Maeda et al. (2011) to use low-frequency
95 seismic waves. We collected data from 70 earthquakes that occurred between 2004 and
96 2019 with moment magnitudes $4.2 \leq Mw \leq 5.8$ and depths shallower than 60 km (Figure1(c),(d)).
97 Earthquake parameters for simulations were extracted from their Global CMT solutions
98 (Ekström et al., 2012); these values were fixed while updating our velocity models, be-
99 cause inversion for source parameter updates requires additional computation time. In
100 addition, we restricted the data to recordings at source–receiver distances of >80 km.

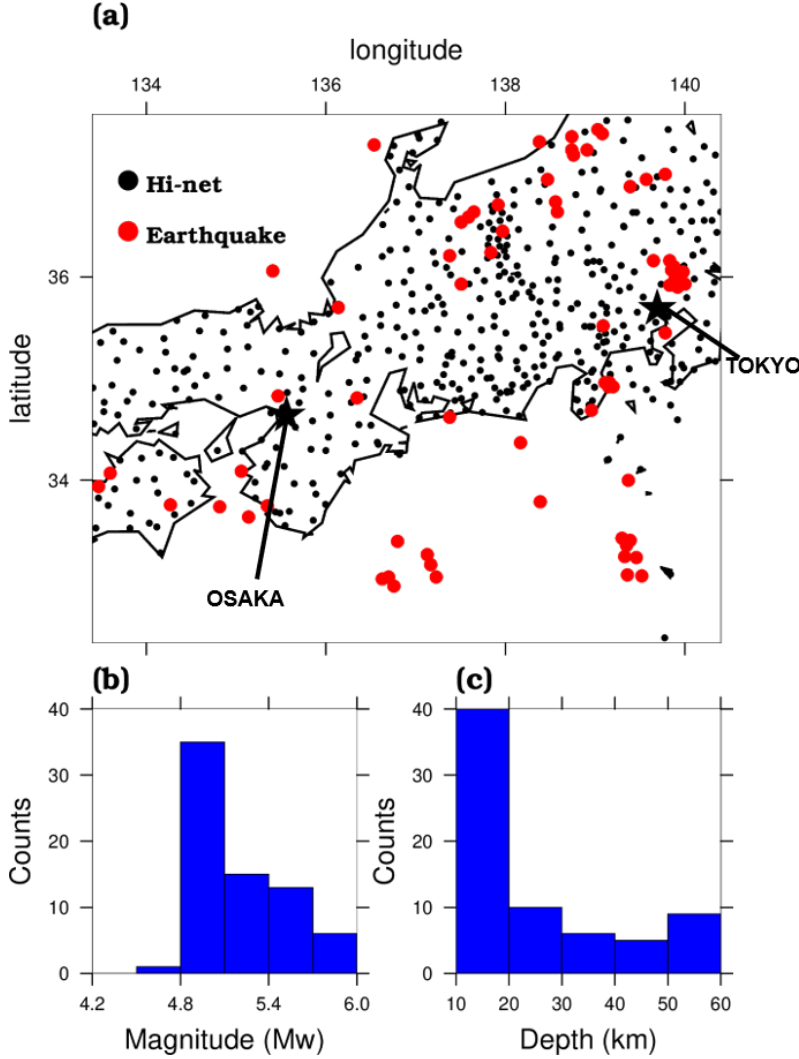


Figure 1. (a) The distributions of seismometers of Hi-net and earthquakes. (b) The magnitude of earthquakes used in this study. (c) The depths of earthquake used in this study.

3 Method

3.1 3D seismic wave simulation and initial model

Synthetic waveforms of 240 sec were calculated using the spectral element method, which is widely used in seismology due to its accuracy and ease of code parallelisation (Komatitsch & Tromp, 1999, 2002; Tape et al., 2010). We used the program SPEC-FEM3D for forward and adjoint 3D isotropic seismic wave simulations (Peter et al., 2011). We selected Lagrange polynomials of degree 5 to represent the seismic wavefield in our target region.

The laterally homogeneous seismic velocity model named JMA2001 was used as the initial model (Ueno et al., 2002); this provides S- and P- wave velocity structures around Japan. We obtained initial density structures using empirical relationship between P-wave velocity and density (Brocher, 2005):

$$\rho = 1.6612V_p - 0.4721V_p^2 + 0.0671V_p^3 - 0.0043V_p^4 + 0.000106V_p^5, \quad (1)$$

114 where ρ is in g/cm^3 and V_p is in km/sec .

115 3.2 Misfit of waveforms

116 Noisy observed data, which is dissimilar to synthetic data, could result in incor-
 117 rect model parameters. In addition, cycle skipping can lead to a local minimum in the
 118 waveform inversion’s solution space that does not correspond to true structure. The lat-
 119 ter phenomenon can occur when observed waveforms are more than half a wavelength
 120 out of phase from synthetic waveforms; therefore, data selection must be carried out as
 121 carefully as possible to prevent this. In this study, we automatically determine the time
 122 windows of pairs of synthetic and observed waveforms based on parameters such as time
 123 lag, the cross-correlation coefficient between observed and synthetic waveforms, and the
 124 signal-to-noise ratio, using the program FLEXWIN (Maggi et al., 2009). We optimized
 125 the model parameters in two frequency ranges: 0.0333–0.1 and 0.0333–0.125 Hz. Thus,
 126 time-window selection was carried out in the first iteration for each frequency range. As
 127 a result, time windows were determined for 21,486 waveform pairs in the 0.033–0.1 Hz
 128 range and 26,934 in the 0.033–0.125 Hz range. The quantification of the misfit between
 129 synthetic and observed waveforms was based on phase misfit using the time-frequency
 130 transform (Fichtner et al., 2008, 2009).

131 3.3 Model update

132 We compute sensitivity kernels with respect to model parameters using the adjoint
 133 method (Fichtner, 2010), then use these in a conjugate-gradient optimization with step
 134 lengths set so that the change from the previous model was always $<6\%$. We use a mul-
 135 tiscale strategy that first recovers the smooth Earth’s structures, then resolve finer-scale
 136 structures by broadening the frequency range (from 0.033–0.1 to 0.033–0.125 Hz). The
 137 most energetic phase in our data is the surface wave; therefore, only the S-wave veloc-
 138 ity was updated between iterations.

139 4 Results and Interpretations

140 After 9 iterations of the 0.033–0.1 Hz band and 3 iterations of the 0.033–0.125 Hz
 141 band we obtained the S-wave velocity model shown in Figure 2. We stopped the inver-
 142 sion in each frequency band when the misfit of the current iteration increased from the
 143 model of the previous iteration. The results show strong horizontal velocity variations:
 144 for example, at 10 km depth, low-velocity anomalies reach <3000 m/s, whereas high-velocity
 145 anomalies are ~ 4000 m/s.

146 The misfit is reduced by 16.5% in the 0.033–0.1 Hz band after 9 iterations and 3.7%
 147 in the 0.033–0.125 Hz band after 3 iterations (Figures 3). We confirmed that the mis-
 148 fits between observed and synthetic waveforms were improved after 12 iterations; rep-
 149 resentative examples are shown in figures 4 and 5. In figure 4, panel A shows that the
 150 waveforms corresponding to the initial model are faster than the observed waveforms;
 151 therefore, the perturbations from the initial model take negative values around the path
 152 between the earthquake and seismometer A (figure 4). In contrast, the perturbation val-
 153 ues are positive around the paths between the earthquake and other seismometers (B,
 154 C, and D, in figure 4). This agrees with the observation that the waveforms correspond-
 155 ing to the initial model in these panels arrive later than the observed waveforms.

156 The largest feature in the resultant S-wave velocity model is that the northern part
 157 of the study area is characterized by low velocities, whereas high velocities dominate in
 158 the south. This general finding agrees with previous studies (J. Nakajima & Hasegawa,
 159 2007a; Nishida et al., 2008). In addition, many earthquakes are distributed at the low-
 160 velocity anomalies (figure 2).

161 At 5 km depth, there is a distinct low-velocity anomaly around region A. The Ni-
162 igata sedimentary basin, which formed during the opening of the Japan Sea (Takano,
163 2002), covers a portion of this low-velocity anomaly. As expected, the thick sedimentary
164 rocks of the Niigata basin yield lower seismic velocities. In addition, multiple active vol-
165 canoes, such as Asama mountain and Kusatsu–Shirane mountain, are in this region. There-
166 fore, the low-velocity anomaly could be due in part to the sedimentary basin as well as
167 magmatic fluids associated with back-arc volcanism.

168 The high-velocity anomaly trending from southwest to northeast is located around
169 the region B at all depth images (figures 2). This anomaly may be associated with the
170 granitic rocks in the Ryoke-belt. Cretaceous low-pressure metamorphic belt located along
171 the north side of the MTL (T. Nakajima, 1994). The anomaly coincides with the Ryoke
172 belt in the Chubu area, and with local granitoids emplaced into the metamorphic rocks
173 of the belt (T. Nakajima, 1994; Ishihara & Chappell, 2007). Thus, igneous rocks that
174 are harder than their surrounding rocks may be responsible for the high velocities in re-
175 gion B.

176 The distributions of velocity anomalies are consistent with the previous velocity
177 model using first-arrival tomography (J. Nakajima & Hasegawa, 2007a). However, for
178 example, the Kanto mountain can be seen clearly as high velocity block at 10 km depth
179 in our results (figure 2), and this feature is not present in the velocity model of J. Naka-
180 jima and Hasegawa (2007a). This could be derived from the larger number of ray paths
181 of J. Nakajima and Hasegawa (2007a) or incorporating surface wave of our inversion. In
182 fact, the high velocity block of Kanto mountain is present in the S-wave velocity model
183 derived from ambient noise tomography using surface wave (Nishida et al., 2008). How-
184 ever, the high velocity anomaly around the Ryoke-belt is more clear than Nishida et al.
185 (2008) and we infer that the result of our study has higher lateral resolution than the
186 velocity model derived only from surface wave.

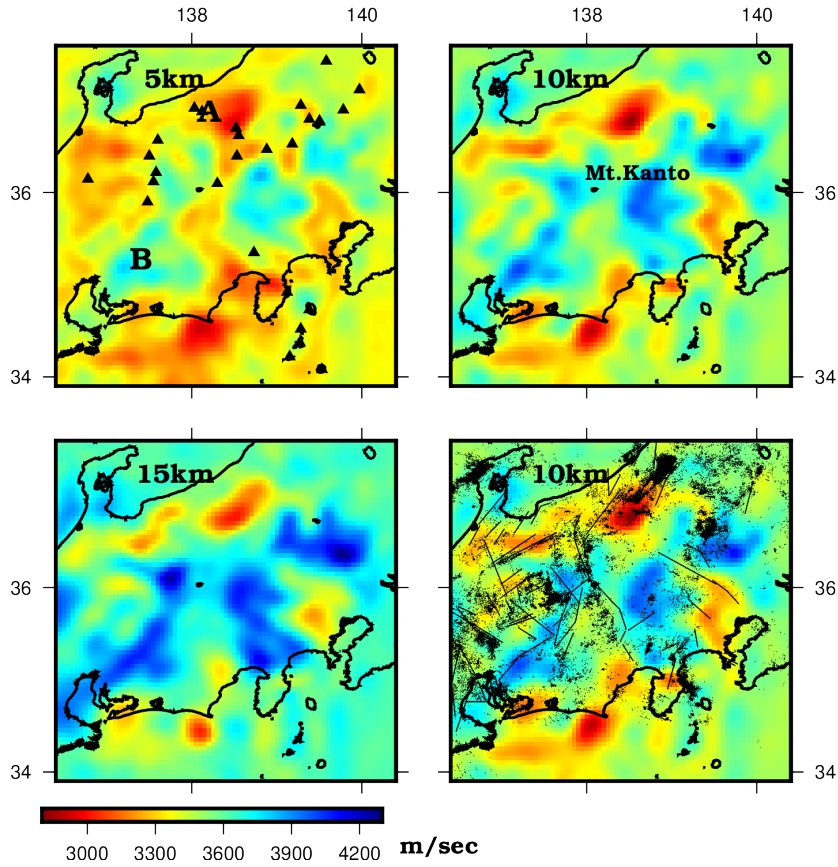


Figure 2. Horizontal slices of the S-wave tomographic model at depths of 5, 10, and 15 km. The bottom-right figure shows the S-wave tomographic model at depth of 15 km with the distributions of faults and earthquakes. We used JUICE catalog (Yano et al., 2017) for the locations of hypocenters. We plotted hypocenters located between 5 and 15 km depth. Black triangles denote volcanoes.

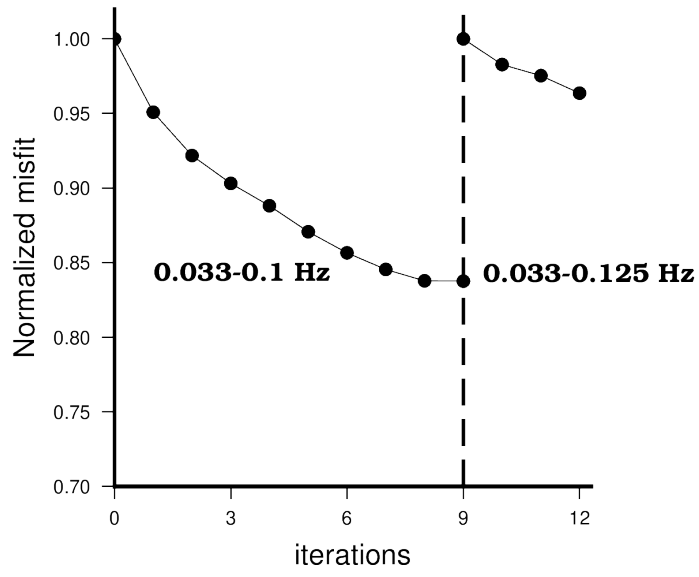


Figure 3. Normalized misfit reductions in the frequency ranges 0.033–0.1 and 0.033–0.125 Hz, respectively.

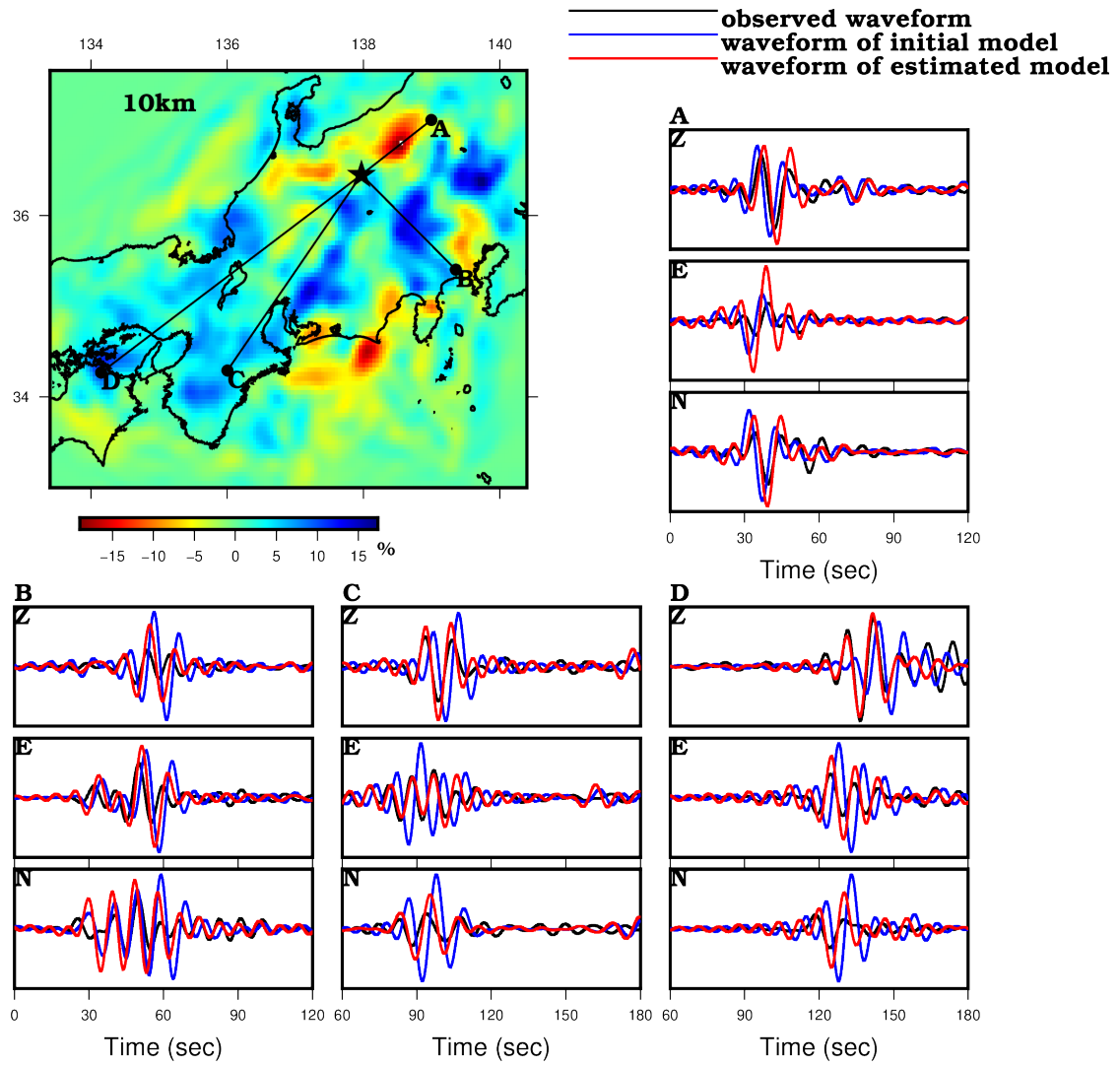


Figure 4. The improvement of waveform fittings. The upper-left subfigure shows velocity perturbations from the initial model at 10 km depth. The black star and circles indicate the epicenters and seismometers, respectively. Panels A–D show observed waveforms (black lines), waveforms of the initial model (blue lines), and waveforms of the final model (red lines), corresponding to the seismometers in the top-left figure. In each panel, vertical (Z), eastward (E), and northward (N) components are shown.

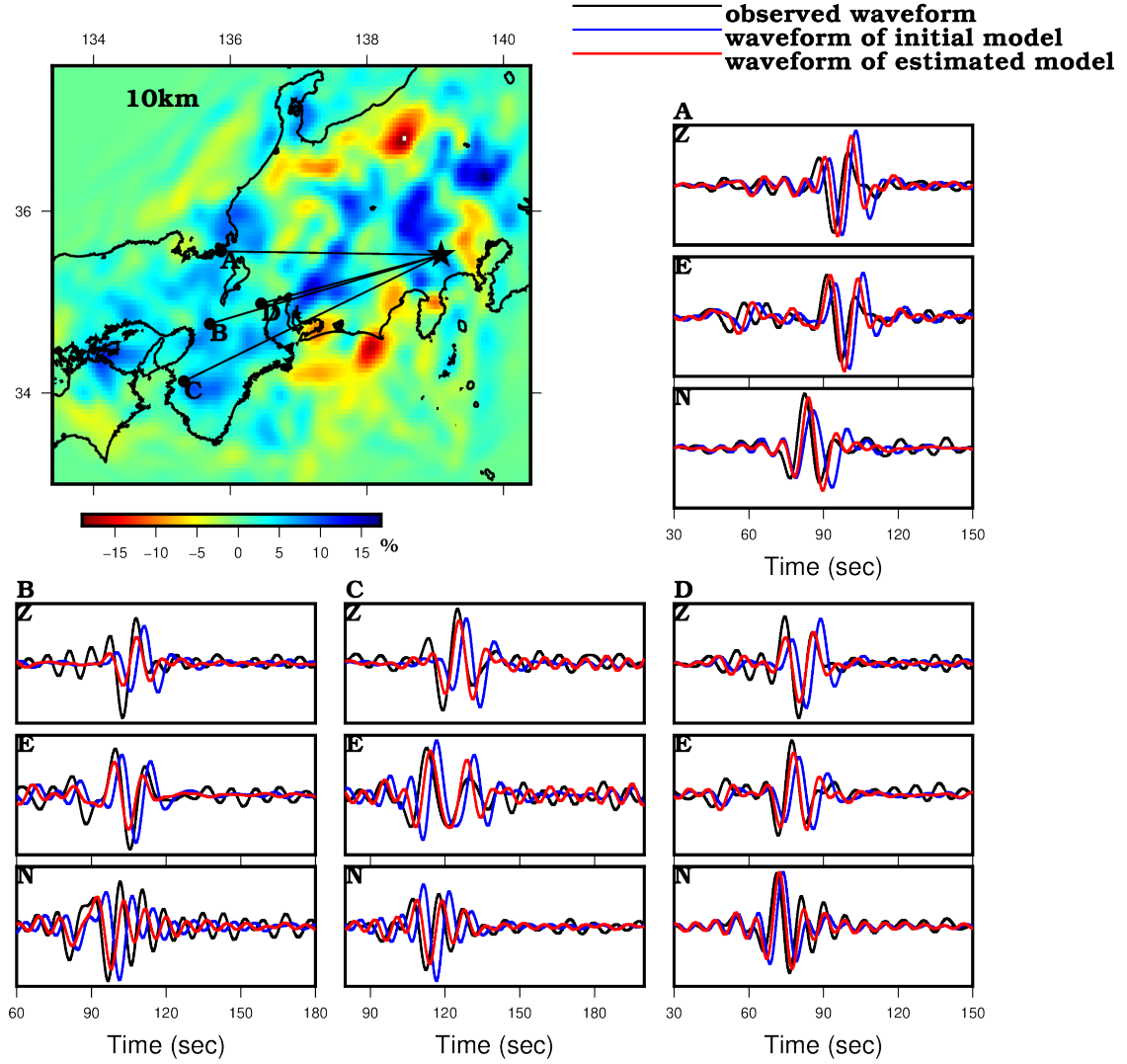


Figure 5. This figure is the same as figure 4 but shows the results of different earthquake-station pairs. The upper-left subfigure shows the velocity perturbation from the initial model at 10 km depth. The black star and circles indicate the epicenters and stations, respectively. Panels A–D show observed waveforms (black lines), waveforms of the initial model (blue lines), and waveforms of the final model (red lines), corresponding to seismometers in the top-left figure. In each panel, vertical (Z), eastward (E), and northward (N) components are shown.

5 Discussion

We conducted a checkerboard test to assess the resolution and reliability of the S-wave velocity model. In this test, cube-shaped anomalies with velocity perturbations of $\pm 18\%$ relative to the background were inserted into the JMA2001 model (figure 6). The area of each anomaly was $35\text{km} \times 35\text{km}$, which is suitable for evaluating the reliability of the high- and low-velocity anomalies resolved in Figure 2. Because our goal was to construct an S-wave velocity model, anomalies were only introduced into S-wave velocity, not P-wave velocity or density. When sensitivity kernels were calculated for the checkerboard test, we used the same time windows for seismogram pairs as those in the

196 model estimation. We then tried to invert the checkerboard model using the JMA2001
197 model without anomalies.

198 Figure 6 shows the results of the checkerboard test sliced at 5, 10, 15, and 20 km
199 depths. We confirm that high-velocity anomalies are less recoverable than low-velocity
200 anomalies at all depths, which was also confirmed in a previous study (Fichtner et al.,
201 2009). At 10 and 15 km depths, the checkerboard pattern is clearer than at other depths.
202 Therefore, our data set (earthquakes and stations) and frequency ranges (0.033–0.1 and
203 0.033–0.125 Hz) seem to be most sensitive to structures at depths of 10–15 km. At 20
204 km depth, sensitivity is lower than at shallower depths. In addition, we confirmed that
205 the checkerboard pattern could not be resolved at depths below 25 km. Therefore, based
206 on our sensitivity test, we conclude that the S-wave velocity structure in figure 2 is re-
207 liable at depths up to 15 km.

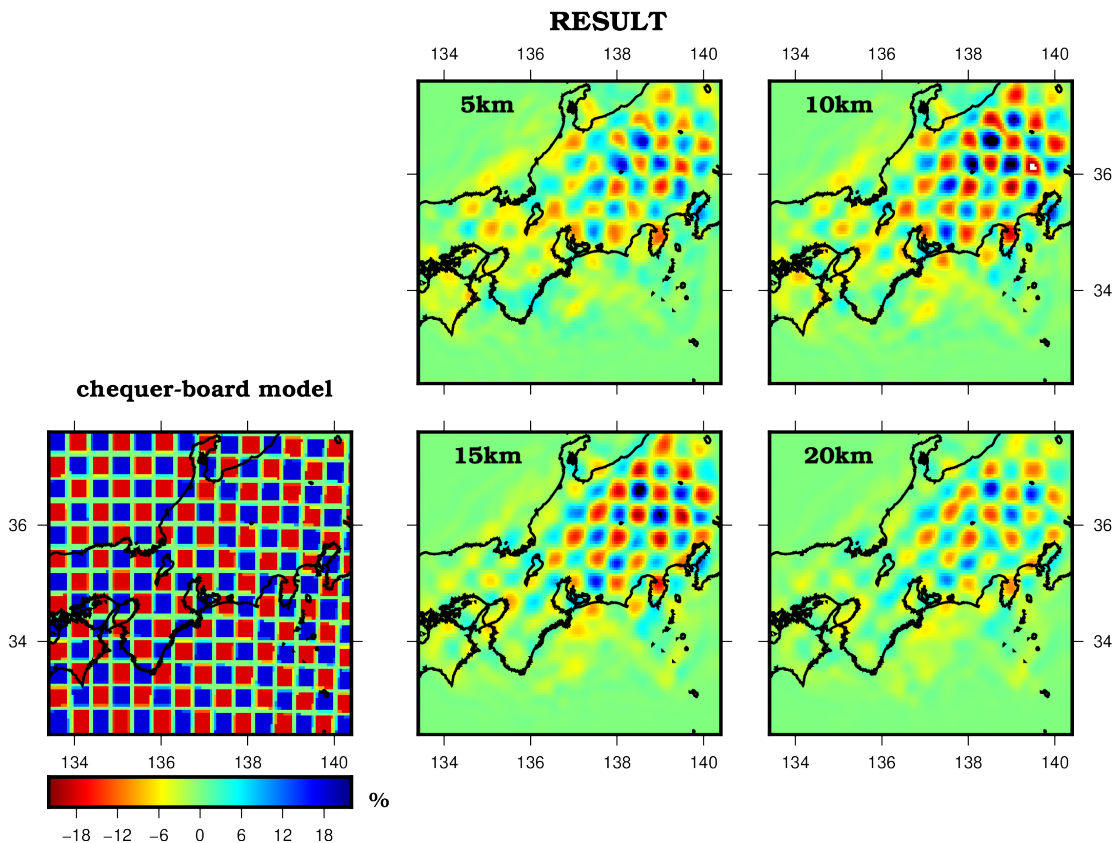


Figure 6. Checkerboard test. The left subfigure shows the checkerboard model used in the resolution test. The remaining four subfigures show the results of the checkerboard test at depth slices of 5, 10, 15, and 20 km, respectively.

208 We estimated 3D S-wave velocity structure in central Japan by exploiting the ad-
209 vantages of adjoint waveform tomography, such as full numerical calculation of seismic
210 wave propagation, 3D sensitivity distributions of seismic waves, and incorporating as many
211 seismic phases as possible. As discussed in section 4, the resultant S-wave velocity model
212 was consistent with the geology and produced waveforms that fit the observed data (fig-
213 ure 4 and 5). Therefore, the new velocity model will increase the accuracy of earthquake
214 source parameter estimates. Previous study confirmed that using a 3D rather than 1D

215 velocity model improves the estimation of earthquake source parameters, owing to the
 216 incorporation of the effects of structural inhomogeneities (Hejrani et al., 2007).

217 6 Conclusions

218 From seismic waveforms from 70 earthquakes recorded by 358 Hi-net seismic stations
 219 we built a 3D S-wave velocity model using adjoint waveform tomography. The model
 220 estimation procedure was designed to minimize the time-frequency phase misfit between
 221 observed and synthetic seismic waveforms in the frequency bands 0.033–0.1 and 0.033–
 222 0.125 Hz. We used conjugate-gradient optimization and obtained a final S-wave velocity
 223 model after 12 iterations. The final model resolves strong horizontal heterogeneities,
 224 with velocity values in the range 2800–4000 m/s. The low-velocity anomalies resolved
 225 in the present work appear to correspond to a thick sedimentary basin and volcanic fluids.
 226 Granitic rocks of the Ryoke belt are plausible causes of the high-velocity anomalies.
 227 Based on a checkerboard test, our data set and frequency ranges are sensitive to depths
 228 of 15 km in the continental region of central Japan. Therefore, we expect that our model
 229 has high accuracy for that region. In addition, the improved fit between observed and
 230 calculated waveforms obtained with our final model supports the accuracy of the results.

231 This study confirms that adjoint waveform tomography and densely distributed Hi-net
 232 stations in Japan can resolve S-wave velocity structure and explain known geology,
 233 yielding results comparable to other velocity models and seismic waveforms similar to
 234 observed data. Although we have not yet confirmed that earthquake data recorded by
 235 Hi-net stations have sufficient resolution for other regions characterized by complex geologic
 236 features, such as Kyushu and Hokkaido, the combination of adjoint waveform tomography
 237 and Hi-net station data will lead to accurate velocity models throughout the
 238 Japanese islands.

239 Acknowledgments

240 This work was supported by the Japan Society for the Promotion of Science (JSPS) through
 241 a Grant-in-Aid for JSPS Research Fellow (JP21J21871). We used the open-source software
 242 SPEC-FEM3D for seismic wave simulation and we thank the developers of SPEC-FEM3D.
 243 We also thank the National Research Institute for Earth Science and Disaster Prevention
 244 (NIED) for providing us with Hi-net data. The Hi-net data is available from <https://hinetwww11.bosai.go.jp/auth/?LANG=en>. The CMT solutions used in this study are
 245 available from <https://www.globalcmt.org/>. Seismic wave simulations were conducted
 246 on the ITO supercomputer system at the Research Institute for Information Technology,
 247 Kyushu University. We used the open-source software GMT (Generic Mapping Tools)
 248 (Wessel et al., 2013) to construct figures. The S-wave velocity model we built is available
 249 at <https://doi.org/10.6084/m9.figshare.14811255.v1>.

251 References

- 252 Arai, R., & Iwasaki, T. (2014). Crustal structure in the northwestern part of the Izu
 253 collision zone in central Japan. *Earth, Planets and Space*, *66*(1), 1–12.
- 254 Arai, R., Iwasaki, T., Sato, H., Abe, S., & Hirata, N. (2013). Crustal structure of
 255 the Izu collision zone in central Japan from seismic refraction data. *Journal of
 256 Geophysical Research: Solid Earth*, *118*(12), 6258–6268.
- 257 Brocher, T. M. (2005). Empirical relations between elastic wavespeeds and density
 258 in the earth’s crust. *Bulletin of the Seismological Society of America*, *95*(6),
 259 2081–2092.
- 260 Ekström, G., Nettles, M., & Dziewoński, A. M. (2012). The global CMT project
 261 2004–2010: Centroid-moment tensors for 13,017 earthquakes. *Physics of the
 262 Earth and Planetary Interiors*, *200*, 1–9.

- 263 Fichtner, A. (2010). *Full seismic waveform modelling and inversion*. Springer Sci-
 264 ence & Business Media.
- 265 Fichtner, A., Kennett, B. L. N., Igel, H., & Bunge, H. P. (2008). Theoretical
 266 background for continental-and global-scale full-waveform inversion in the
 267 time–frequency domain. *Geophysical Journal International*, *175*(2), 665–685.
- 268 Fichtner, A., Kennett, B. L. N., Igel, H., & Bunge, H. P. (2009). Full seismic wave-
 269 form tomography for upper-mantle structure in the australasian region using
 270 adjoint methods. *Geophysical Journal International*, *179*(3), 1703–1725.
- 271 Fichtner, A., Kennett, B. L. N., Igel, H., & Bunge, H. P. (2010). Full waveform to-
 272 mography for radially anisotropic structure: new insights into present and past
 273 states of the australasian upper mantle. *Earth and Planetary Science Letters*,
 274 *290*(3-4), 270–280.
- 275 Hejrani, B., Tkalčić, H., & Fichtner, A. (2007). Centroid moment tensor catalogue
 276 using a 3-d continental scale earth model: Application to earthquakes in papua
 277 new guinea and the solomon islands. *Journal of Geophysical Research: Solid*
 278 *Earth*, *122*(7), 5517–5543.
- 279 Ishihara, S., & Chappell, B. W. (2007). Chemical compositions of the late cretaceous
 280 ryoike granitoids of the chubu district, central japan–revisited. *Bulletin of the*
 281 *Geological Survey of Japan*, *58*(9/10), 323–350.
- 282 Komatitsch, D., & Tromp, J. (1999). Introduction to the spectral element method
 283 for three-dimensional seismic wave propagation. *Geophysical journal interna-*
 284 *tional*, *139*(3), 806–822.
- 285 Komatitsch, D., & Tromp, J. (2002). Spectral-element simulations of global seismic
 286 wave propagation—i. validation. *Geophysical Journal International*, *149*(2),
 287 390–412.
- 288 Lei, W., Ruan, Y., Bozdağ, E., Peter, D., Lefebvre, M., Komatitsch, D., ... Pug-
 289 mire, D. (2020). Global adjoint tomography model glad-m25. *Geophysical*
 290 *Journal International*, *223*(1), 1–21.
- 291 Maeda, T., Obara, K., Furumura, T., & Saito, T. (2011). Interference of long-period
 292 seismic wavefield observed by the dense hi-net array in japan. *Journal of Geo-*
 293 *physical Research: Solid Earth*, *116*(B10).
- 294 Maggi, A., Tape, C., Chen, M., Chao, D., & Tromp, J. (2009). An automated time-
 295 window selection algorithm for seismic tomography. *Geophysical Journal Inter-*
 296 *national*, *178*(1), 257–281.
- 297 Miyoshi, T., Obayashi, M., Peter, D., Tono, Y., & Tsuboi, S. (2017). Adjoint tomog-
 298 raphy of the crust and upper mantle structure beneath the kanto region using
 299 broadband seismograms. *Progress in Earth and Planetary Science*, *4*(1), 1–20.
- 300 Nakajima, J., & Hasegawa, A. (2007a). Deep crustal structure along the niigata-
 301 kobe tectonic zone, japan: Its origin and segmentation. *Earth, planets and*
 302 *space*, *59*(2), e5–e8.
- 303 Nakajima, J., & Hasegawa, A. (2007b). Subduction of the philippine sea plate
 304 beneath southwestern japan: Slab geometry and its relationship to arc magmat-
 305 ism. *Journal of Geophysical Research: Solid Earth*, *112*(B8).
- 306 Nakajima, J., Hirose, F., & Hasegawa, A. (2009). Seismotectonics beneath the tokyo
 307 metropolitan area, japan: Effect of slab-slab contact and overlap on seismicity.
 308 *Journal of Geophysical Research: Solid Earth*, *114*(B8).
- 309 Nakajima, T. (1994). The ryoike plutonometamorphic belt: crustal section of the cre-
 310 taceous eurasian continental margin. *Lithos*, *33*(1-3), 51–66.
- 311 Nimiya, H., Ikeda, T., & Tsuji, T. (2020). Three-dimensional s wave velocity struc-
 312 ture of central japan estimated by surface-wave tomography using ambient
 313 noise. *Journal of Geophysical Research: Solid Earth*, *125*(4), e2019JB019043.
- 314 Nishida, K., Kawakatsu, H., & Obara, K. (2008). Three-dimensional crustal s
 315 wave velocity structure in japan using microseismic data recorded by hi-net
 316 tiltmeters. *Journal of Geophysical Research: Solid Earth*, *113*(B10).
- 317 Okada, Y., Kasahara, K., Hori, S., Obara, K., Sekiguchi, S., Fujiwara, H., & Ya-

- 318 mamoto, A. (2004). Recent progress of seismic observation networks in japan
319 -hi-net, f-net, k-net and kik-net-. *Earth, Planets and Space*, *56*(8), xv–xxviii.
- 320 Peter, D., Komatitsch, D., Luo, Y., Martin, R., Goff, N. L., Casarotti, E., . . .
321 Tromp, J. (2011). Forward and adjoint simulations of seismic wave propa-
322 gation on fully unstructured hexahedral meshes. *Geophysical Journal Interna-*
323 *tional*, *186*(2), 721–739.
- 324 Simutè, S., Steptoe, H., Cobden, L., Gokhberg, A., & Fichtner, A. (2016). Full-
325 waveform inversion of the japanese islands region. *Journal of Geophysical Re-*
326 *search: Solid Earth*, *121*(5), 3722–3741.
- 327 Takano, O. (2002). Changes in depositional systems and sequences in response to
328 basin evolution in a rifted and inverted basin: an example from the neogene
329 niigata-shin’etsu basin, northern fossa magna, central japan. *Sedimentary*
330 *Geology*, *152*(1-2), 79–97.
- 331 Tape, C., Liu, Q., Maggi, A., & Tromp, J. (2010). Seismic tomography of the south-
332 ern california crust based on spectral-element and adjoint methods. *Geophysi-*
333 *cal Journal International*, *180*(1), 433–462.
- 334 Ueno, H., Hatakeyama, S., Aketagawa, T., Funasaki, J., & Hamada, N. (2002). Im-
335 provement of hypocenter determination procedures in the japan meteorological
336 agency (in japanese). *Q. J. Seismol*, *65*, 123–134.
- 337 Wessel, P., Smith, W., Scharroo, R., Luis, J., & Wobbe, F. (2013). Generic map-
338 ping tools: improved version released. *Eos, Transactions American Geophysical*
339 *Union*, *94*(45), 409–410.
- 340 Yano, T. E., Takeda, T., Matsubara, M., & Shiomi, K. (2017). Japan unified high-
341 resolution relocated catalog for earthquakes (juice): crustal seismicity beneath
342 the japanese islands. *Tectonophysics*, *702*, 19–28.